Supplementary Information (SI) for Energy & Environmental Science.
This journal is © The Royal Society of Chemistry 2026

Supporting Information

Entropy-Regulated Dielectric Friction in Eutectic Electrolyte Unlocks 150°C High-Performance Li Metal Batteries

Yaodong Huo[a], Duanduan Li[a], Chunkun Song[a], Qiyue Zhao[a], Yongqi Wang[a], Yong Gao[a], Tuotuo Ma [*b], Xiaojun Gu[*a], Yuliang Gao[*a]

[a]School of Chemistry and Chemical Engineering, Inner Mongolia University, Hohhot 010021, China

[b]School of Physical Science and Technology, Inner Mongolia University, Hohhot 010021, China

E-mail: ttma@imu.edu.cn; xiaojun.gu@imu.edu.cn; ylgao@imu.edu.cn

Materials

Difluoromethyl 2-pyridyl sulfone (FMPS, 98%) was obtained from Tianjin Heowns Biochemical Technology Co., Ltd. Lithium (fluorosulfonyl)(trifluoromethanesulfonyl)imide (LiFTSI, 99%) was obtained from Gaoxin District Lebo Chemical Products Management Department. Lithium bis(fluorosulfonyl)imide (LiFSI, 99.5%), lithium bis(trifluoromethanesulfonyl)imide (LiTFSI, 99.5%), lithium tetrafluoroborate ($LiBF_4$, 99.5%), $LiFePO_4$ (99%), polyvinylidene fluoride (PVDF, grade 900), Super P conductive carbon, Al foil (16 μm), Cu foil (10 μm), and Li sheets (500 μm) were purchased from Guangdong Canrd New Energy Technology Co., Ltd. V_2O_5 (99%), trifluoromethanesulfonamide ($TfNH_2$, 98%), 3,4,5-trifluorobenzenesulfonyl chloride (98%), 4-bromo-3,5-difluorobenzenesulfonyl chloride (97%), and N-methyl-2-pyrrolidone (NMP, 99.5%) were purchased from Beijing MREDA Technology Co., Ltd. Potassium carbonate (K_2CO_3, 99%), anhydrous acetonitrile (99%), dichloromethane (99%), and anhydrous diethyl ether (99%) were obtained from Tianjin Fengchuan Chemical Reagent Technology Co., Ltd.

Synthesis of lithium (3,4,5-trifluorobenzenesulfonyl)(trifluoromethanesulfonyl)imide (LiFFF) and lithium (4-bromo-3,5-difluorobenzenesulfonyl)(trifluoromethanesulfonyl)imide (LiFBF)

As previously reported,[1] CF_3SO_2NHK (3 g, 16.03 mmol) and K_2CO_3 (5.09 g, 36.87 mmol with respect to CF_3SO_2NHK) were stirred in acetonitrile (100 mL) for 30 min. Subsequently, 3,4,5-trifluorobenzenesulfonyl chloride (3.99 g, 17.31 mmol) was added to the suspension, and the reaction mixture was stirred for 36 h. Then centrifuged the product and collected the supernatant. The solvent was removed by rotary evaporation to yield a white solid (KFFF).

To obtain the LiFFF salt, KFFF (1 g, 2.62 mmol) and $LiBF_4$ (0.212 g, 2.62 mmol) were stirred in acetonitrile (20 mL) for 30 min to facilitate cation exchange. After that, the precipitate was removed by centrifugation. The solvent was evaporated, and the resulting solid was washed with diethyl ether and dichloromethane, followed by drying under vacuum at 80°C to afford the high-purity LiFFF salt.

LiFBF was synthesized following the same procedure as for LiFFF, except that 3,4,5-trifluorobenzenesulfonyl chloride was replaced with 4-bromo-3,5-difluorobenzenesulfonyl chloride.

Preparation of eutectic electrolytes

Three eutectic electrolytes were prepared in an argon-filled glovebox (H_2O and O_2 contents < 0.5 ppm). The high-entropy eutectic electrolyte (HEEE) was obtained by heating FMPS with LiFSI, LiFTSI, LiTFSI, LiFFF, and LiFBF at a molar ratio of 8:0.2:0.2:0.2:0.2:0.2 at 80°C for 1 h. For comparison, the medium entropy eutectic electrolyte (MEEE) and the monocomponent eutectic electrolyte (MEE) were prepared following the same procedure, using molar ratios of 8:0.33:0.33:0.33

(FMPS:LiFSI:LiFTSI:LiTFSI) and 8:1 (FMPS:LiTFSI), respectively. The commercial electrolyte of 1 M $LiPF_6$ in DEC/EMC/EC (1:1:1 by volume) was purchased from Canrd and used as the reference.

Preparation of $LiFePO_4$ and V_2O_5 cathodes

Commercial $LiFePO_4$ (LFP), Super P, and PVDF were mixed in a mass ratio of 7:2:1 and ground in an agate mortar for 30 min. The mixture was then dispersed in NMP and stirred for 12 h to yield a homogeneous slurry, which was subsequently coated onto Al foil. After vacuum drying at 80°C, LFP electrode sheets with an active material loading of approximately 1.0 mg cm^{-2} were obtained. V_2O_5 electrode sheets are prepared in the same way.

Physicochemical characterizations

The morphology of lithium electrodeposition was characterized by scanning electron microscopy (SEM, Hitachi S-4800). The microstructure of the electrolytes was investigated using Fourier transform infrared spectroscopy (FTIR, Bruker Tensor 27) and Raman spectroscopy (UHTS 600 SMFC VIS, 532 nm). Nuclear magnetic resonance (NMR, JEOL JNM-ECZL400S) analysis was performed on electrolyte solutions prepared in deuterated dimethyl sulfoxide. Solidification points of the various electrolytes were determined by differential scanning calorimetry (DSC, Netzsch DSC 200 F3) under nitrogen atmosphere at a heating rate of 5 °C min^{-1}. Viscosity measurements of the electrolytes were conducted using a rotational rheometer (Waters DHR-2) over a temperature range from 30 to 150°C. Dielectric constants and dielectric losses were evaluated by broadband dielectric impedance spectroscopy (Novocontrol Concept 80). Thermogravimetric analysis (TGA) was performed on a thermal analyzer (Netzsch STA 499) under flowing nitrogen (50 mL min^{-1}) at a heating rate of 10 °C min^{-1}. The chemical composition of the SEI was analyzed by X-ray photoelectron spectroscopy (XPS, PHI 5802), and all binding energies were calibrated with reference to the C 1s peak at 284.8 eV.

Electrochemical measurements

2032-type coin cells (Li||Cu cells, Li||Li cells, LFP||Li cells and V_2O_5||Li cells) were assembled with 80 μL of electrolyte in an argon-filled glovebox. All cells were tested using NEWARE battery testing systems. Room temperature (25°C) measurements were performed with the MIHW-200-160CH-B, while high temperature (80, 120 and 150°C) tests were conducted with the CT4008Tn in an electrothermal constant temperature drying oven. V_2O_5||Li cells were tested at 25 and 150°C in the voltage range of 2.5~3.2 V. Tafel plots, linear sweep voltammetry (LSV), electrochemical impedance spectroscopy (EIS, 0.1 Hz~100 kHz), ionic conductivity measurements, and cyclic voltammetry (CV) were performed on an electrochemical workstation (CHI 760E). Infrared thermal imaging experiment was conducted using specially assembled Li||Li cells. Specifically, the cells were assembled using a positive coin cell case with a drilled observation window to enable direct monitoring of the temperature evolution inside the cell. During the measurement, the opening was sealed with adhesive tape to prevent

air exposure. The assembled cells were then placed on a hot plate maintained at 80°C for 30 min, and the temperature variation in the exposed region was recorded using an infrared thermal imaging camera.

The ionic conductivity of the electrolytes were determined by EIS measurements using stainless steel symmetric cells under potentiostatic mode with an AC amplitude of 5 mV. Ionic conductivity was calculated according to the following Formula (1):

$$\sigma = \frac{L}{R \times S} \tag{1}$$

where L is the thickness of separator, R represents the resistance of cell, and S represents the area of stainless steel.

The corresponding activation energy (E_a) of different electrolytes were accurately fitted based on the Arrhenius equation, represented by Formula (2):

$$\frac{1}{R_{ct}} = A\exp\left(\frac{-E_a}{RT}\right) \tag{2}$$

where R_{ct} is the charge transfer resistance, A is the exponential prefactor, R is the molar gas constant, and T is the absolute temperature.

The Li^+ transference number (t_{Li^+}) was calculated from the chronoamperometry curve recorded at a constant polarization potential of 20 mV for 5000 s, the Formula (3) as follows:

$$t_{Li^+} = \frac{I_S(\Delta V - I_0 R_0)}{I_0(\Delta V - I_S R_S)} \tag{3}$$

where I_0 is the initial current, I_S is the steady-state current, ΔV is the applied potential, and R_0 and R_S are the resistances of the symmetric cell before and after polarization, respectively.

Computational methods

Molecular dynamics (MD) simulations were performed using the Forcite module within the BIOVIA software package, employing the COMPASS III force field. Electrostatic and van der Waals (VDW) interactions were treated using the Ewald and atom-based summation methods, respectively.

Representative solvation structures were extracted from extensive atomistic simulations and used as initial configurations for subsequent density functional theory (DFT) calculations. All DFT calculations were carried out with the Gaussian 16 software package. Geometry optimizations were conducted at the B3LYP level using the 6-311G(d,p) basis set, which is well known for its high accuracy and has been widely applied in previous studies.

Finite element simulations were performed using COMSOL Multiphysics 6.2 with the tertiary current distribution physics interface. The electric field and Li^+ concentration field at the electrode/electrolyte interface were modeled to evaluate the influence of ion-transport behavior on Li deposition. Ion transport was described by diffusion and electromigration. Specifically, diffusion was governed by Fick's law, while electromigration was described by the Nernst-Planck equation. A simplified two-dimensional electrode/electrolyte interfacial model was constructed. The length of each

electrode was set to 10 μm, and the distance between the two electrodes was 6 μm. To mimic the initial surface roughness of the Li metal anode, five triangular protrusions with a base width of 0.4 μm and a height of 0.3 μm were introduced on the anode surface as preferential nucleation sites. The cathode was defined as the zero-potential reference, while a polarization potential corresponding to the operating voltage of the cell was applied to the anode. The initial Li^+ concentration was set to 1 M. The Li^+ diffusion coefficients in the electrolytes were set to 8×10^{-15} m^2 s^{-1}, 5×10^{-15} m^2 s^{-1}, and 1.5×10^{-15} m^2 s^{-1}, respectively. The exchange current density was set to 0.05 mA cm^{-2}, and the system temperature was set to 298 K.

It should be noted that the simulation was used to qualitatively illustrate the effect of ion-transport uniformity on Li deposition behavior, rather than to quantitatively reproduce the exact morphology of Li deposits. Since Li electrodeposition is highly sensitive to the local Li^+ concentration and electric-field distribution near surface protrusions, small differences in ion transport can be amplified at the electrode/electrolyte interface, resulting in different deposition tendencies.

According to the Butler-Volmer Formula (4), the local current density can be calculated as follows:

$$i_{loc} = i_0\left(\exp\left(\frac{\alpha_a F\eta}{RT}\right) - \exp\left(\frac{-\alpha_c F\eta}{RT}\right)\right) \quad (4)$$

where i_{loc} is the current density of electrode, i_0 represents the exchange current density, α_a represents the charge transfer coefficient in the anode direction, α_c represents the charge transfer coefficient in the cathode direction, F is the Faraday constant, η is the activation overpotential, R represents the ideal gas constant, and T is the temperature in Kelvin.

The diffusion and electric field migration Formula (5) was used to study the ion migration:

$$N_{Zn} = -D_{Li}\nabla c_{Li} - Z_{Li}\mu_{m,Li}Fc_{Li}\nabla\Phi_l \quad (5)$$

where N_{Zn} is the Li^+ diffusion flux, D_{Li} represents the Li^+ diffusion coefficient, ∇c_{Li} is the Li^+ concentration gradient, Z_{Li} is the Li^+ band charge, $\mu_{m,Li}$ represents the mobility of Li^+, and $\nabla\Phi_l$ represents the electric potential in solution.

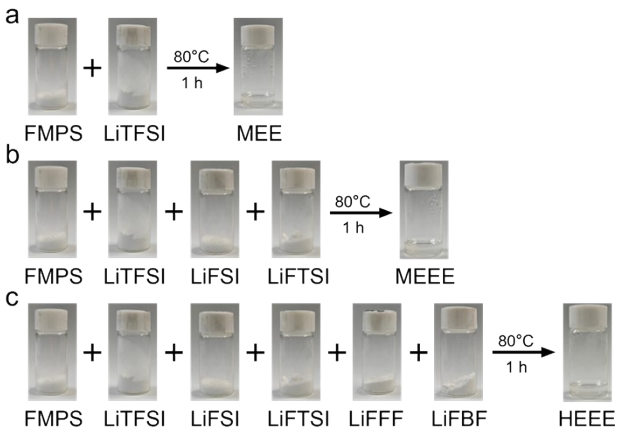

Figure S1. Preparation processes and optical photos of (a) MEE, (b) MEEE and (c) HEEE.

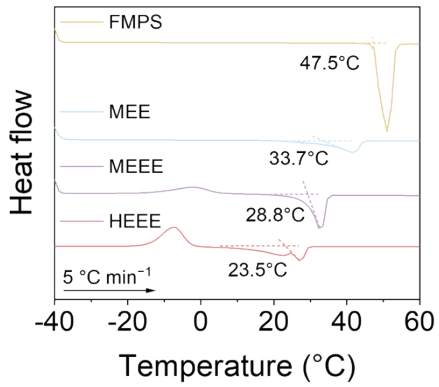

Figure S2. DSC curves of FMPS, MEE, MEEE and HEEE.

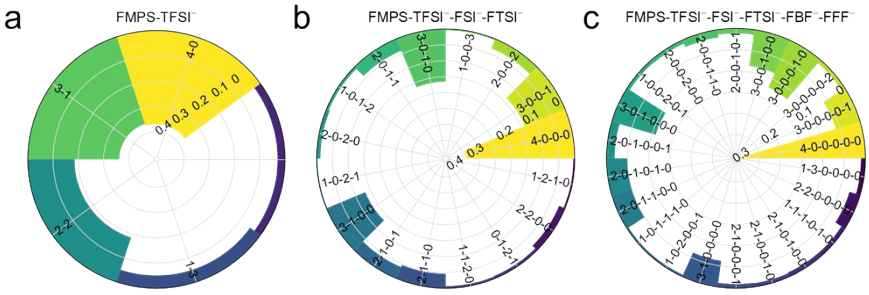

Figure S3. Li^+ coordination environments of (a) MEE, (b) MEEE and (c) HEEE from MD simulations.

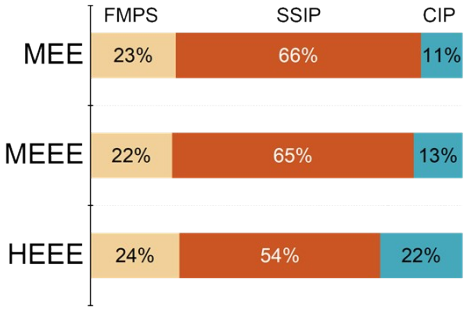

Figure S4. Relative contents of FMPS, SSIP and CIP in different electrolytes.

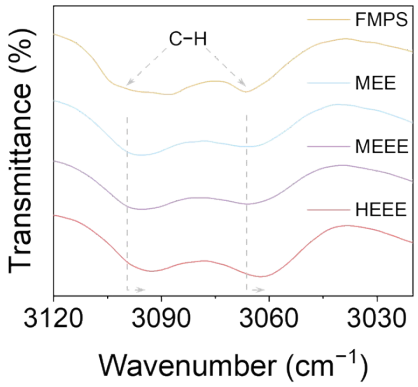

Figure S5. FTIR spectra of FMPS, MEE, MEEE and HEEE.

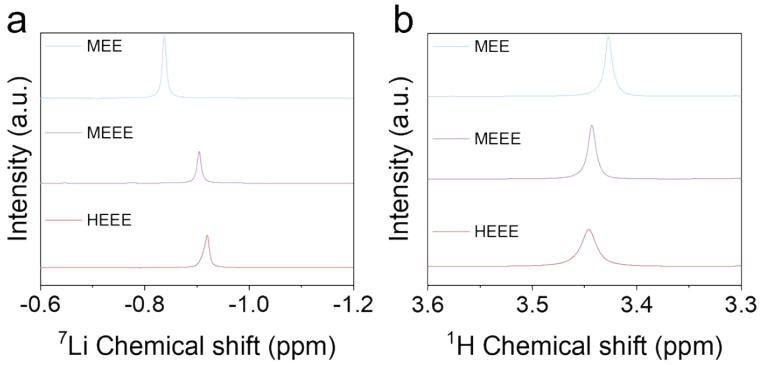

Figure S6. (a) ^{7}Li NMR and (b) ^{1}H NMR spectra of MEE, MEEE and HEEE.

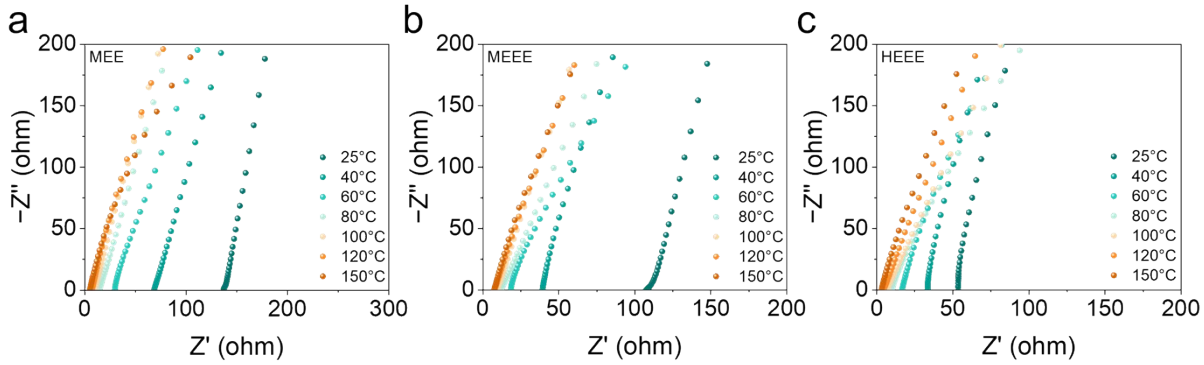

Figure S7. EIS of stainless steel||stainless steel cells with (a) MEE, (b) MEEE and (c) HEEE at different temperatures.

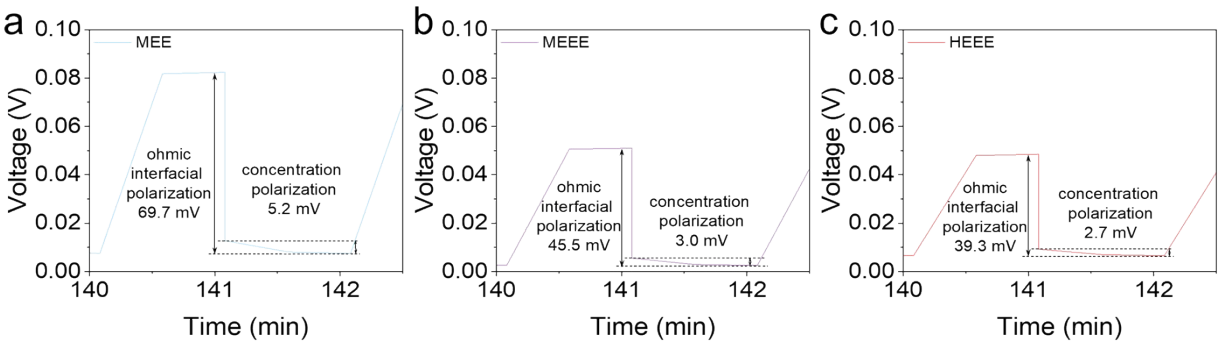

Figure S8. GITT analysis of Li||Li cells with (a) MEE, (b) MEEE and (c) HEEE.

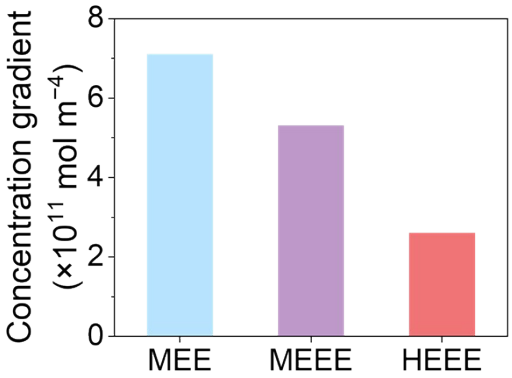

Figure S9. Ion concentration gradient on the anode surface in different electrolytes.

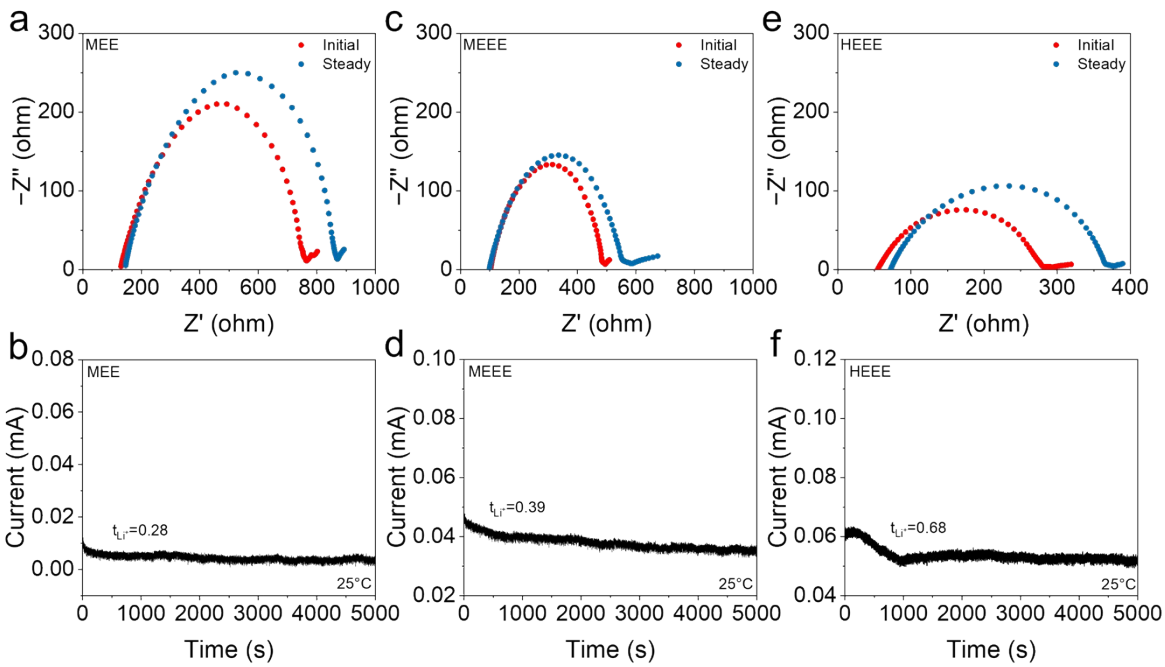

Figure S10. (a, c, e) EIS of Li||Li cells before and after polarization and (b, d, f) chronoamperometry profiles at a polarization voltage of 20 mV in different electrolytes.

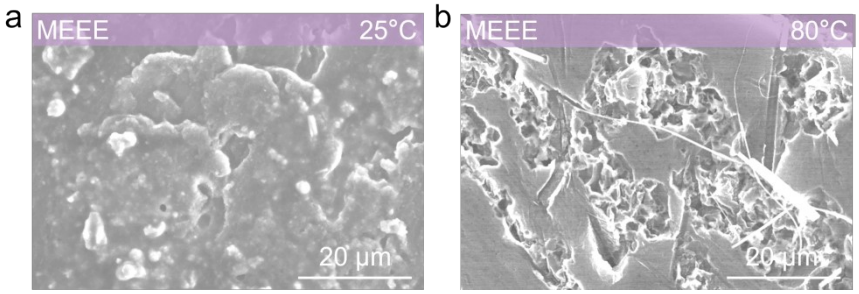

Figure S11. SEM images of Li deposits (2 mAh cm^{-2}) with MEEE at (a) 25 and (b) 80°C.

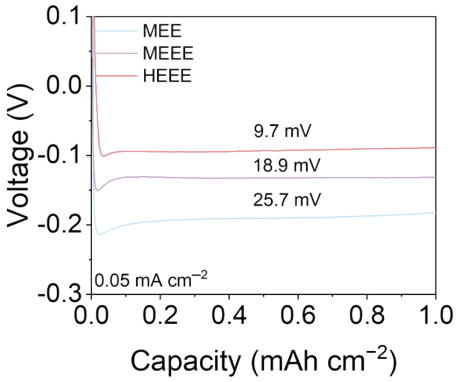

Figure S12. Voltage-capacity curves of Li||Cu cells with different electrolytes.

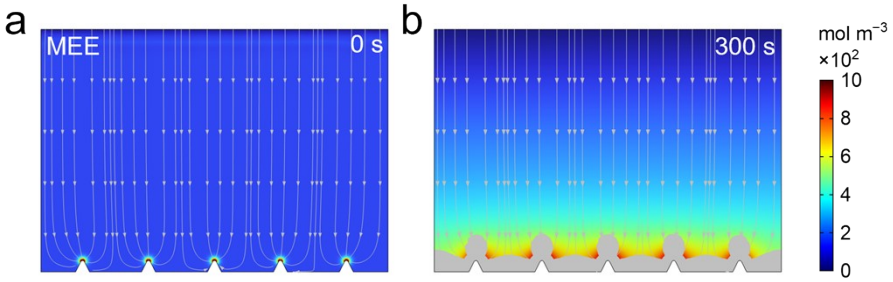

Figure S13. COMSOL simulations of ion distributions and morphological evolution of the electrode surface at (a) 0 and (b) 300 s of Li electrodeposition with MEE.

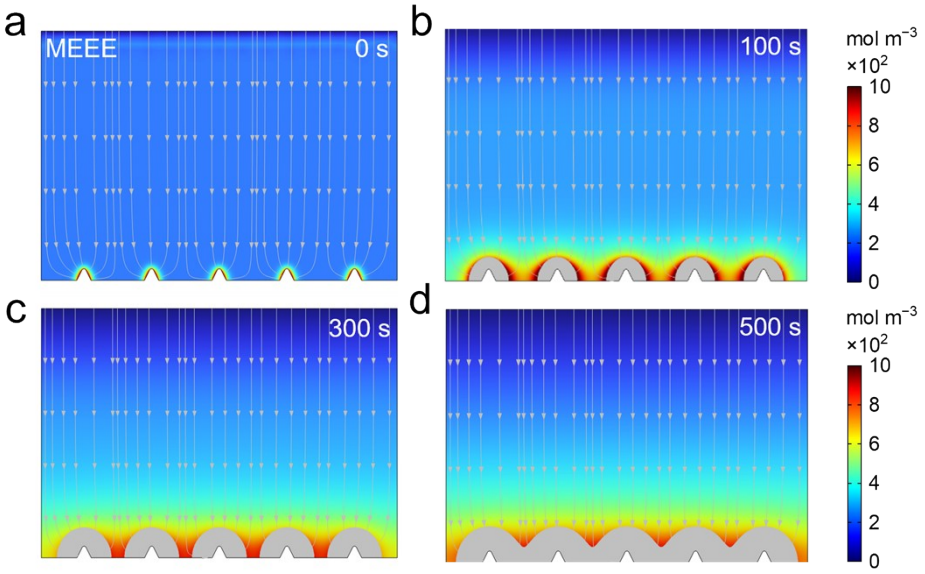

Figure S14. COMSOL simulations of ion distributions and morphological evolution of the electrode surface at (a) 0, (b) 100, (c) 300 and (d) 500 s of Li electrodeposition with MEEE.

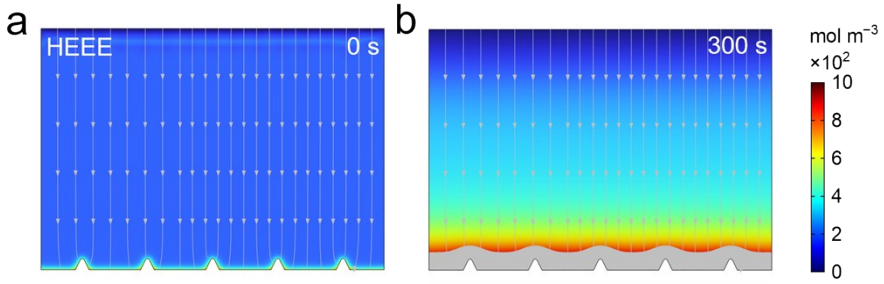

Figure S15. COMSOL simulations of ion distributions and morphological evolution of the electrode surface at (a) 0 and (b) 300 s of Li electrodeposition with HEEE.

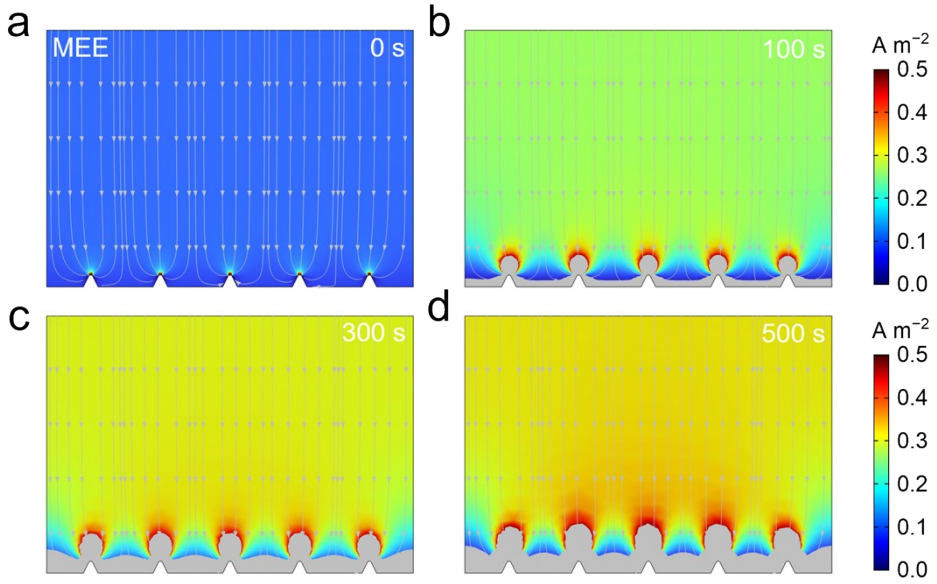

Figure S16. COMSOL simulations of electric field distributions and morphological evolution of the electrode surface at (a) 0, (b) 100, (c) 300 and (d) 500 s of Li electrodeposition with MEE.

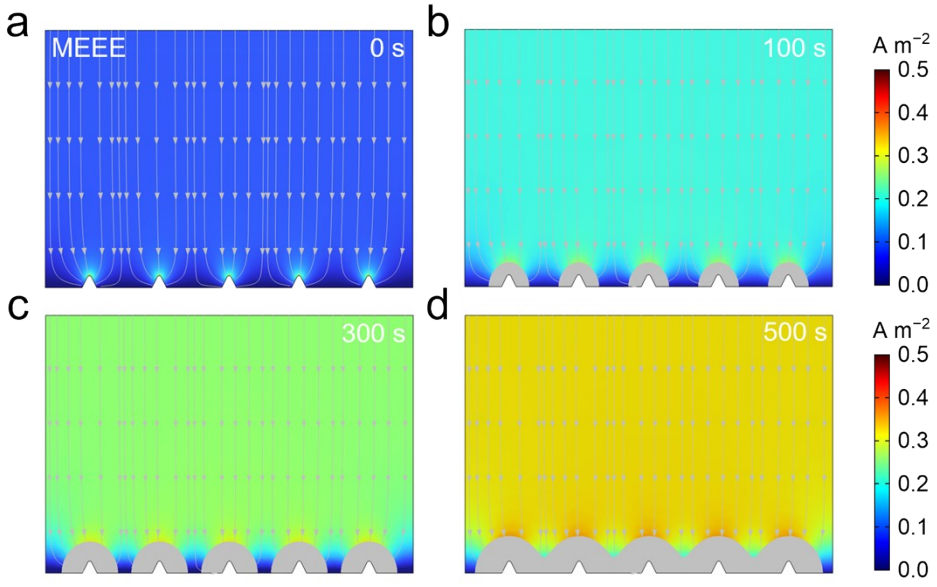

Figure S17. COMSOL simulations of electric field distributions and morphological evolution of the electrode surface at (a) 0, (b) 100, (c) 300 and (d) 500 s of Li electrodeposition with MEEE.

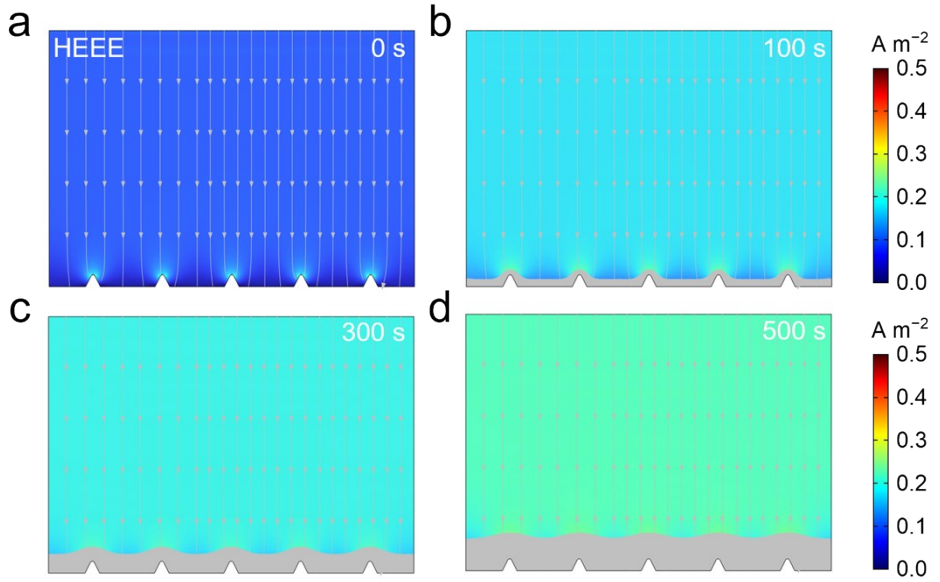

Figure S18. COMSOL simulations of electric field distributions and morphological evolution of the electrode surface at (a) 0, (b) 100, (c) 300 and (d) 500 s of Li electrodeposition with HEEE.

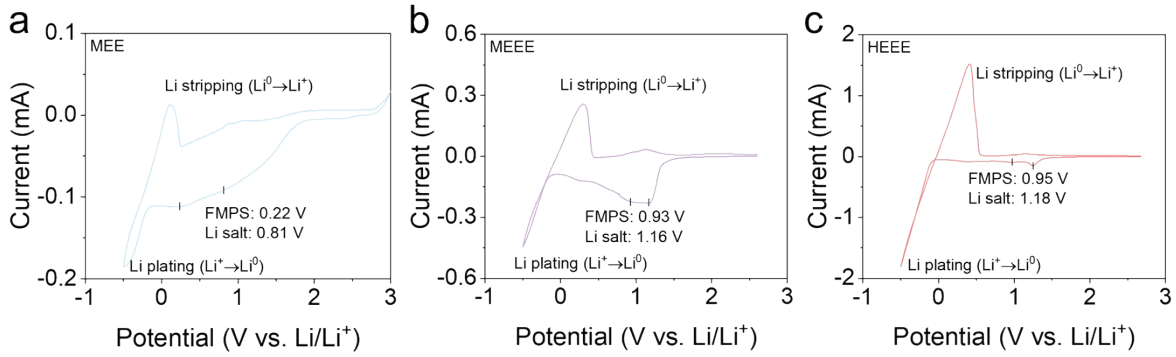

Figure S19. CV curves of (a) MEE, (b) MEEE and (c) HEEE at a scan rate of 0.1 mV s^{-1}.

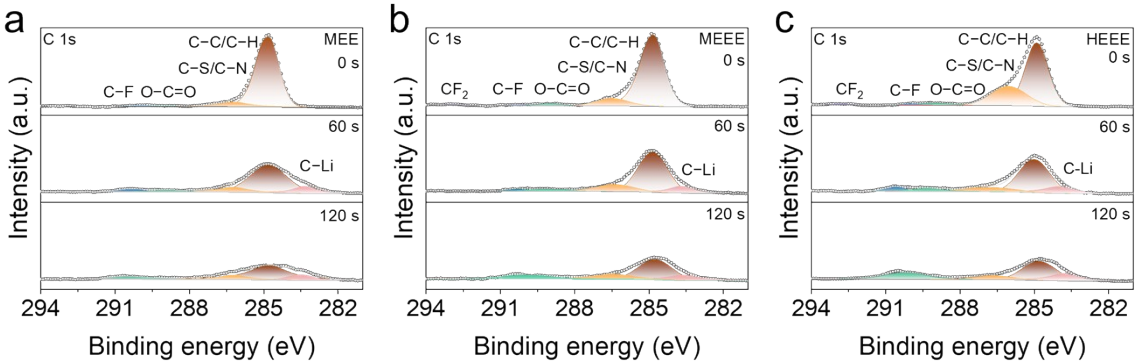

Figure S20. XPS spectra of C 1s in (a) MEE, (b) MEEE and (c) HEEE.

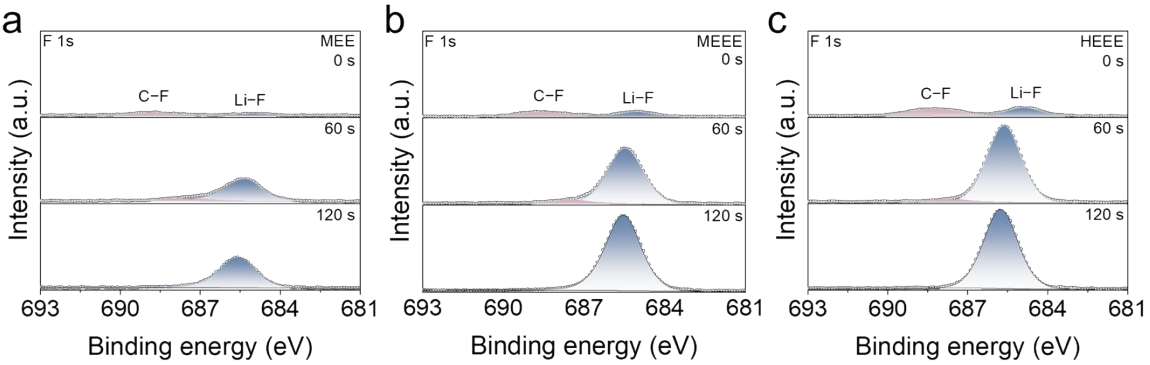

Figure S21. XPS spectra of F 1s in (a) MEE, (b) MEEE and (c) HEEE.

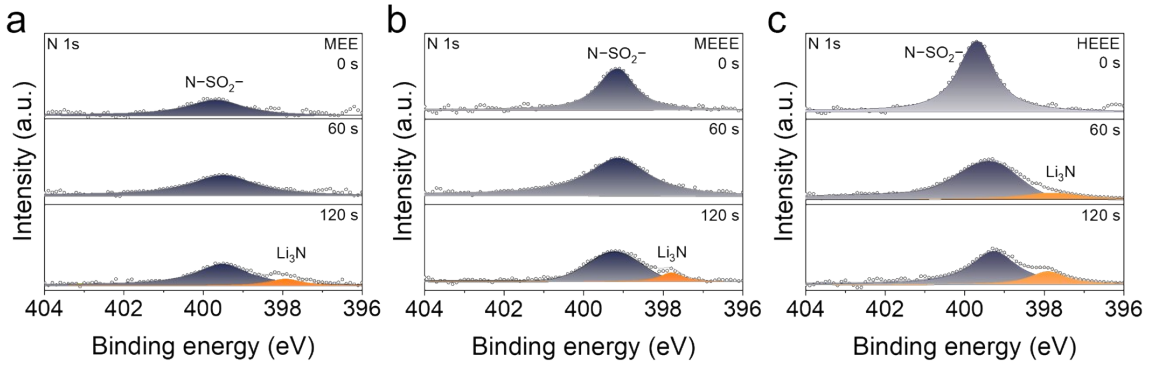

Figure S22. XPS spectra of N 1s in (a) MEE, (b) MEEE and (c) HEEE.

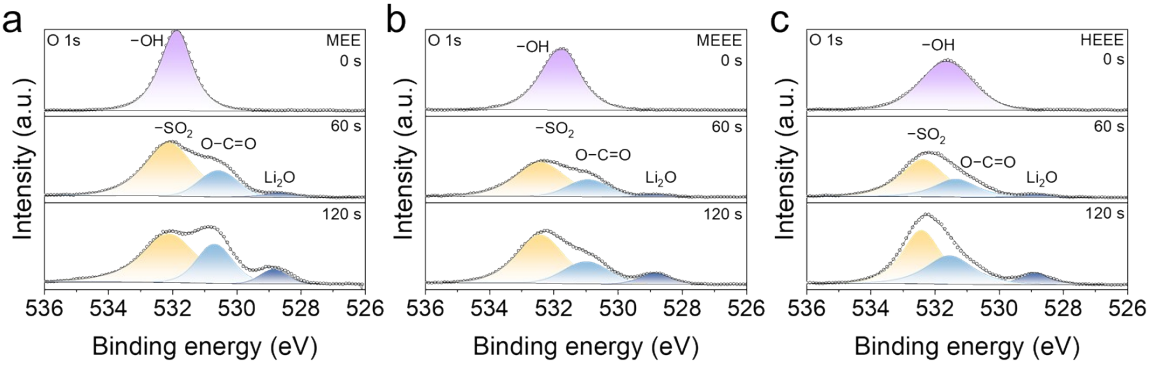

Figure S23. XPS spectra of O 1s in (a) MEE, (b) MEEE and (c) HEEE.

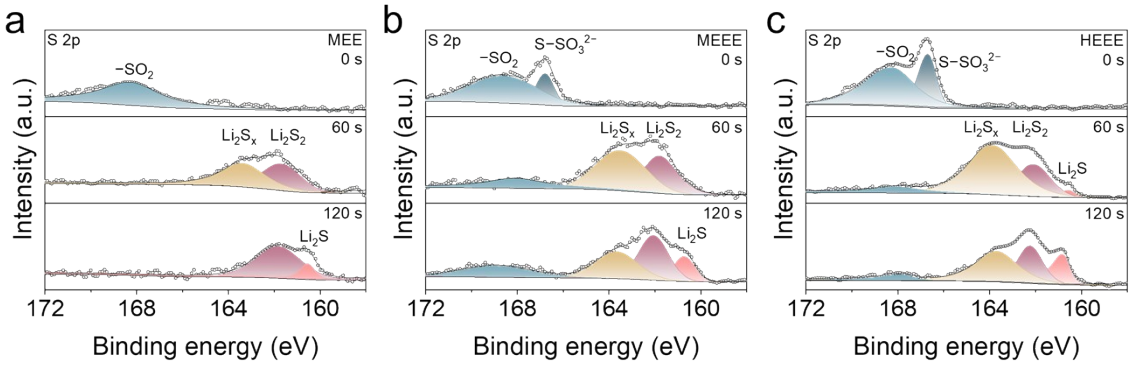

Figure S24. XPS spectra of S 2p in (a) MEE, (b) MEEE and (c) HEEE.

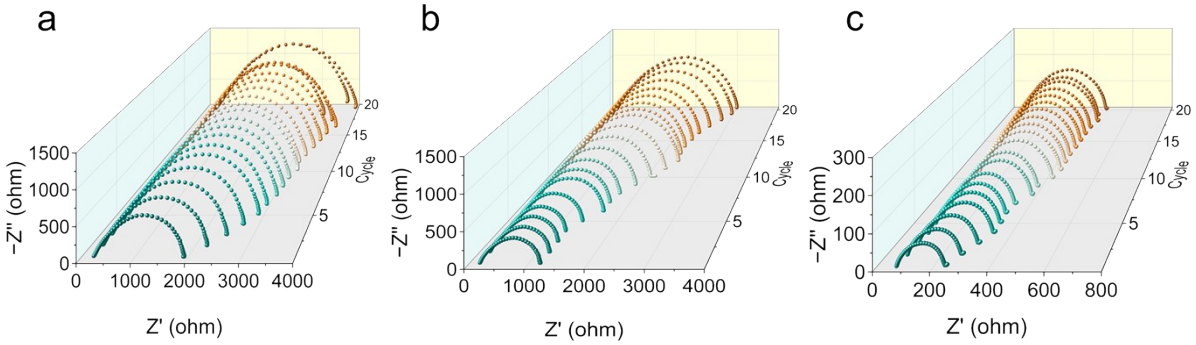

Figure S25. In-situ EIS of Li||Li cells with (a) MEE, (b) MEEE and (c) HEEE.

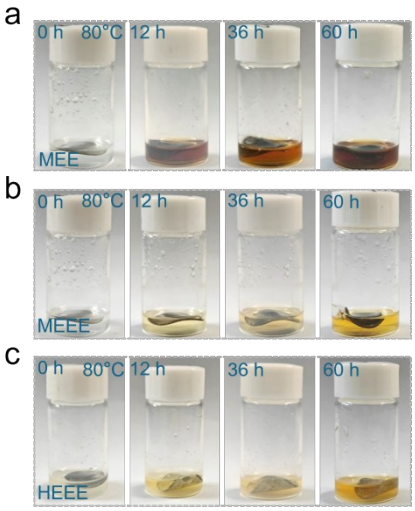

Figure S26. Optical photos of Li sheets immersed in (a) MEE, (b) MEEE and (c) HEEE after storage at 80°C for different times.

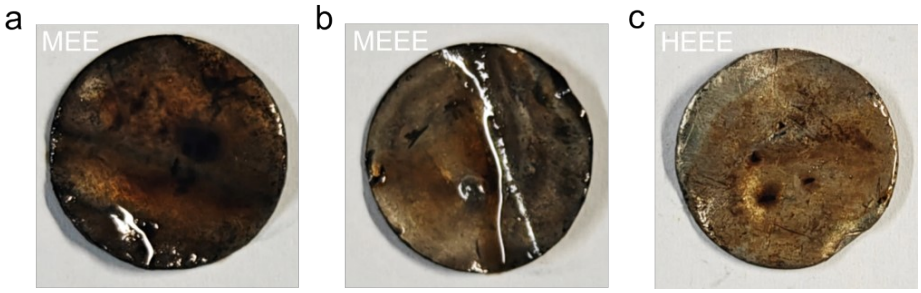

Figure S27. Optical photos of Li sheets after immersion for 60 h in (a) MEE, (b) MEEE and (c) HEEE.

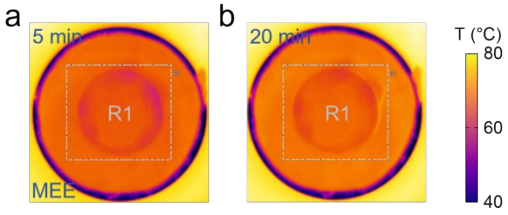

Figure S28. Infrared thermal images of Li||Li cell with MEE at (a) 5 and (b) 20 min during resting at 80°C.

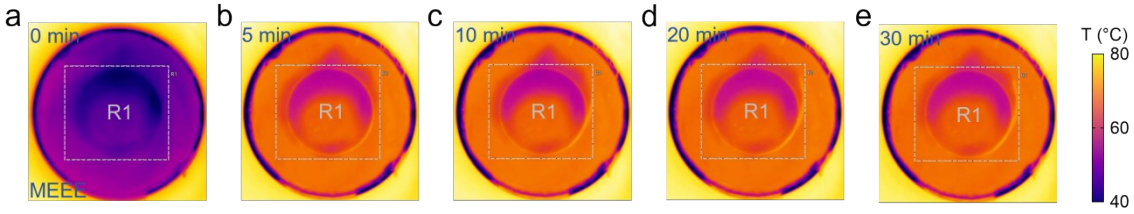

Figure S29. Infrared thermal images of Li||Li cell with MEEE at (a) 0, (b) 5, (c) 10, (d) 20 and (e) 30 min during resting at 80°C.

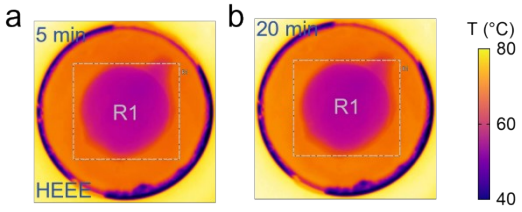

Figure S30. Infrared thermal images of Li||Li cell with HEEE at (a) 5 and (b) 20 min during resting at 80°C.

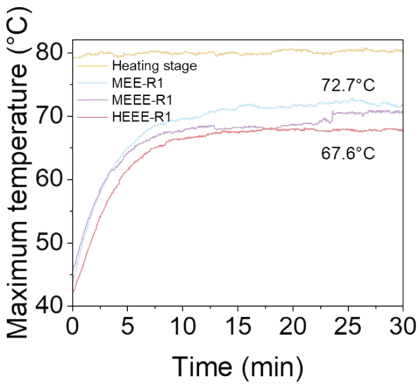

Figure S31. Time-temperature curves from infrared thermal imaging.

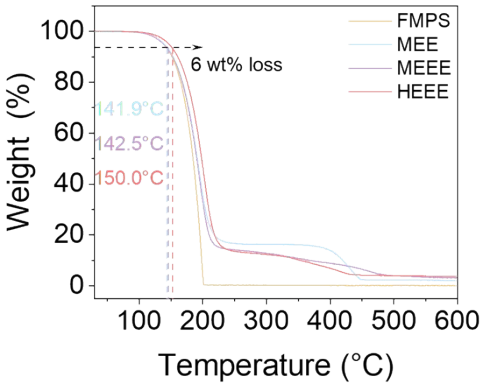

Figure S32. TGA curves of FMPS, MEE, MEEE and HEEE under nitrogen atmosphere.

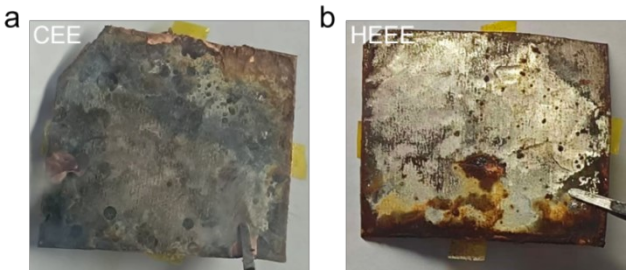

Figure S33. Optical photos of Li metal electrodes retrieved from Li||Li pouch cells with (a) CEE and (b) HEEE after 8 h of storage at 120°C.

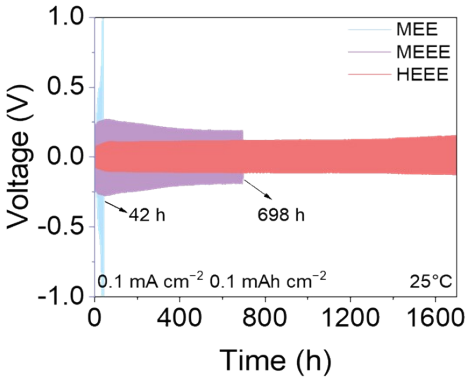

Figure S34. Cycling performance of Li||Li cells at 25°C.

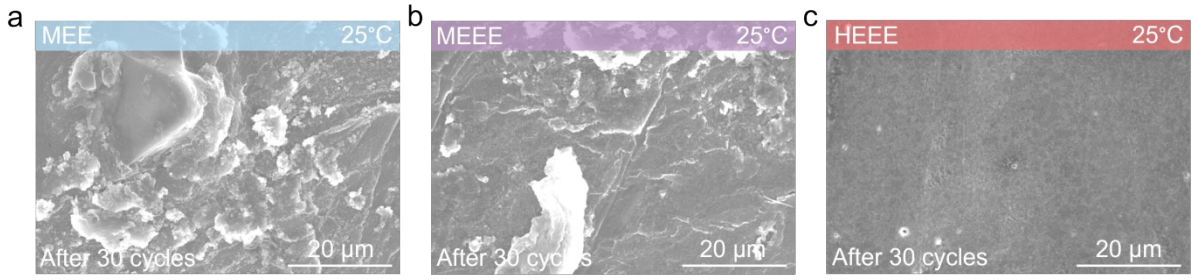

Figure S35. SEM images of Li metal anodes after 30 cycles in Li||Li cells with (a) MEE, (b) MEEE and (c) HEEE at 0.1 mA cm^{-2}/0.1 mAh cm^{-2} at 25°C.

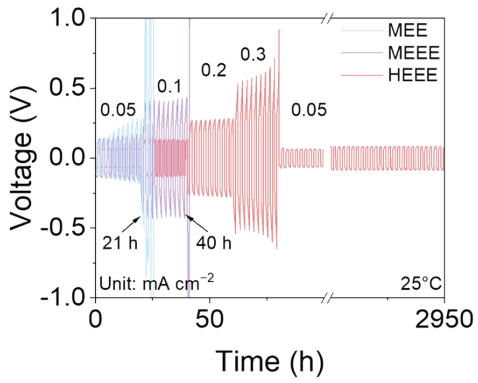

Figure S36. Rate performance of Li||Li cells at 25°C.

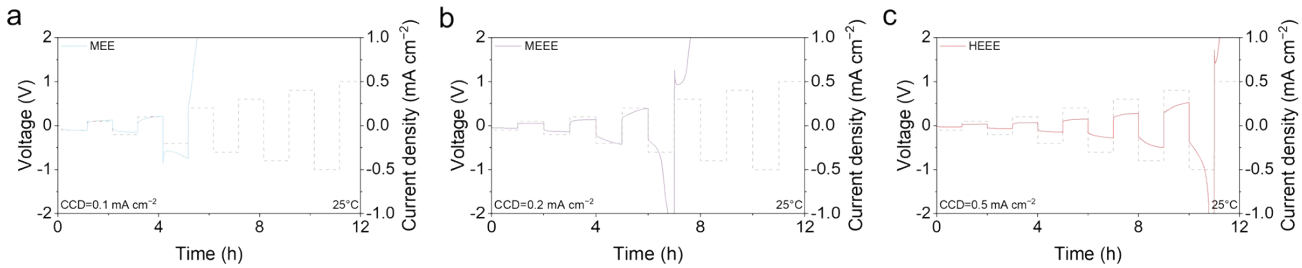

Figure S37. Critical current density tests of Li||Li cells with (a) MEE, (b) MEEE and (c) HEEE at 25°C.

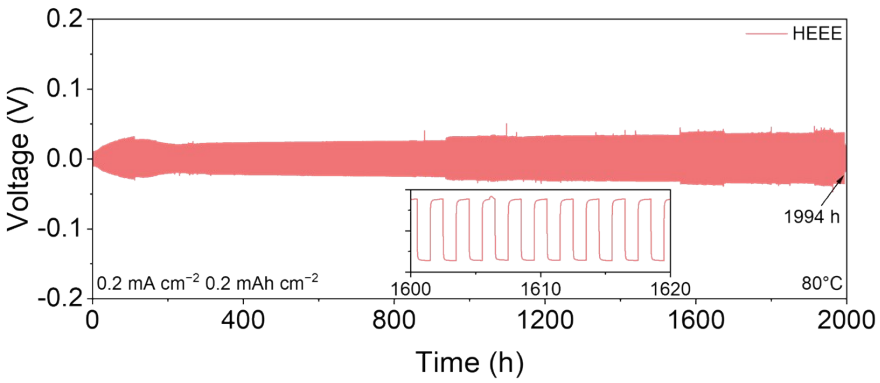

Figure S38. Cycling performance of Li||Li cell with HEEE at 80°C (insert: enlarged view of the selected cycles)

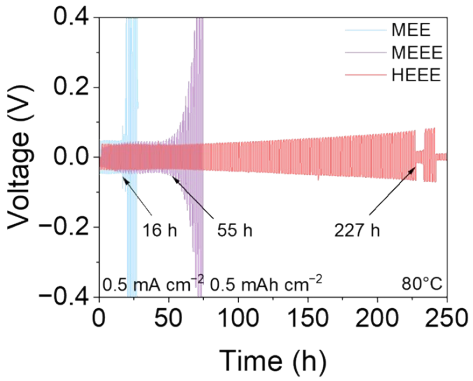

Figure S39. Cycling performance of Li||Li cell with HEEE at 80°C

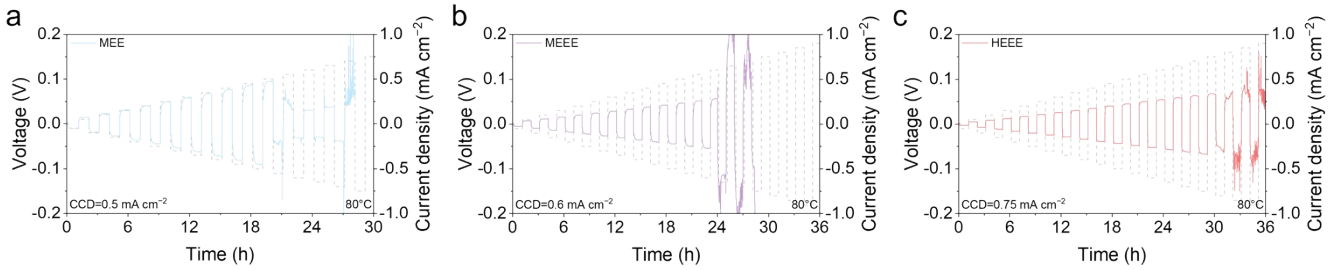

Figure S40. Critical current density tests of Li||Li cells with (a) MEE, (b) MEEE and (c) HEEE at 80°C.

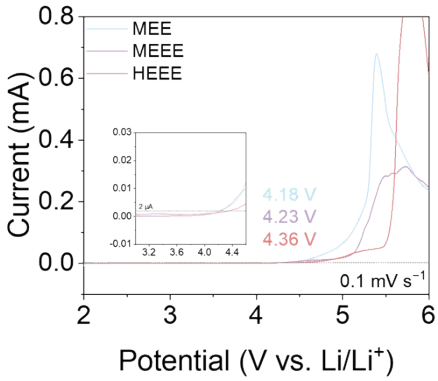

Figure S41. LSV curves of MEE, MEEE and HEEE (insert: enlarged view of the curves near the inflection point).

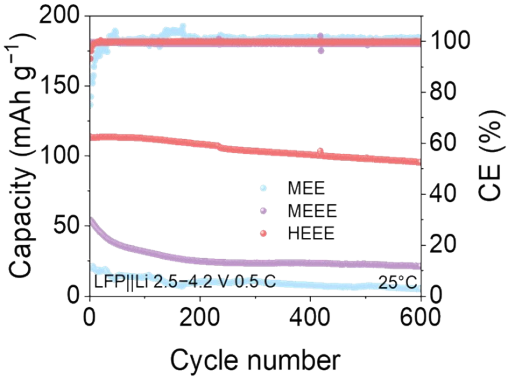

Figure S42. Cycling performance of LFP||Li cells at 25°C.

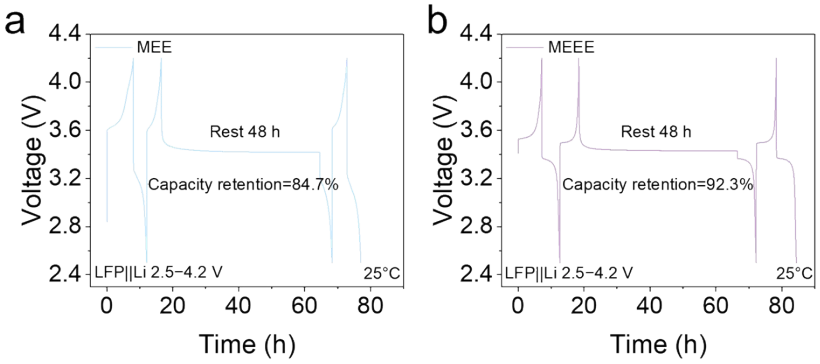

Figure S43. Self-discharge tests of LFP||Li cells with (a) MEE and (b) MEEE.

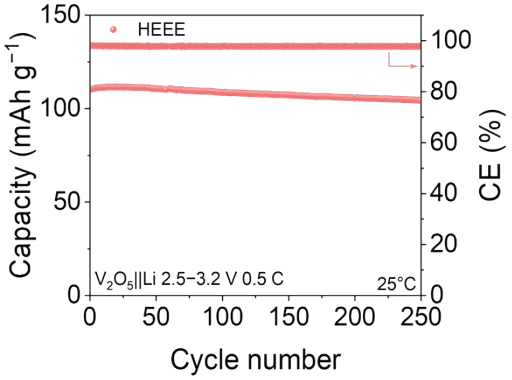

Figure S44. Cycling performance of V_2O_5||Li cell with HEEE at 25°C.

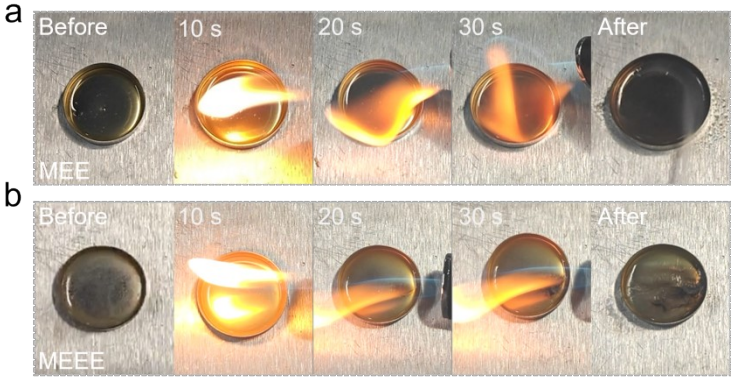

Figure S45. Optical photos of (a) MEE and (b) MEEE combustion test.

Figure S46. Optical photo of LFP||Li pouch cell after nail penetration.

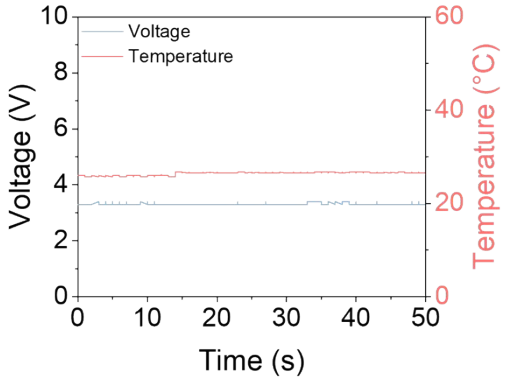

Figure S47. Voltage and temperature curves of the LFP||Li pouch cell during nail penetration.

Table S1. Design parameters of LFP||Li pouch cell.

Design parameter	Value
Capacity	1.07 Ah
Charge-discharge voltage range	2.50~3.65 V
Electrode area (cathode)	55×73 mm
Electrode area (anode)	57×75 mm
LFP loading	18.5 mg cm^{-2}
Li foil	50 μm
Electrolyte volume	4 mL
N/P ratio	3.89

Reference

[1] S. Yan, F. Liu, Y. Ou, et al., "Asymmetric trihalogenated aromatic lithium salt induced lithium halide rich interface for stable cycling of all-solid-state lithium batteries," *ACS Nano*, **17** (2023): 19398–19409, https://doi.org/10.1021/acsnano.3c07246.